Avalanches dynamics in reaction fronts in disordered flows

T. Chevalier,[1] A. K. Dubey,[1] S. Atis,[1] A. Rosso,[2] D. Salin,[1] and L. Talon[1]
[1]*Laboratoire FAST, Université Paris–Sud, CNRS, Université Paris–Saclay, F-91405 Orsay, France*
[2]*LPTMS, Université Paris–Sud, CNRS, Université Paris–Saclay, F-91405 Orsay, France*
(Received 7 September 2016; published 17 April 2017)

We report on numerical studies of avalanches of an autocatalytic reaction front in a porous medium. The front propagation is controlled by an adverse flow resulting in upstream, static, or downstream regimes. In an earlier study focusing on front shape, we identified three different universality classes associated with this system by following the front dynamics experimentally and numerically. Here, using numerical simulations in the vicinity of the second-order transition, we identify an avalanche dynamics characterized by power-law distributions of avalanche sizes, durations, and lateral extensions. The related exponents agree well with the quenched-Kardar-Parisi-Zhang theory, which describes the front dynamics. However, the geometry of the propagating front differs slightly from that of the theoretical one. We show that this discrepancy can be understood in terms of the nonquasistatic correction induced by the finite front velocity.

DOI: 10.1103/PhysRevE.95.042210

I. INTRODUCTION

Interface motion and autocatalytic front propagation occur in many different areas, including chemical reactions [1], population dynamics in biology [the celebrated and pioneering works of Fisher [2] and Kolmogorov-Petrovskii-Piskunov [3] (F-KPP)], and flame propagation in combustion. In contrast to the latter, where it has been analyzed thoroughly theoretically and experimentally [4], the effect of fluid flow (laminar or turbulent) on reaction fronts has not been explored in detail until recently [5–15]. More complex flows have been addressed in recent experiments in packed-bed reactors, i.e., a porous medium [16,17], or in a cellular flow [18].

In the absence of a flow, autocatalytic reactions lead to fronts propagating as solitary waves with a constant velocity and invariant, flat, concentration profile resulting from a balance between reaction and diffusion [1–3]. These reactions are analogous to flames in combustion [4] but with a negligible heat production [19], and thus they represent a kind of "cold combustion model", especially in the thin flame limit. In the presence of a hydrodynamic flow, it has already been observed and understood that such fronts, while propagating at a new constant velocity, adapt their shape in order to achieve a balance between reaction diffusion and flow advection all over the front [7,9].

An autocatalytic reaction in the fluid flow of local velocity $\vec{U}$ is governed by the advection-diffusion-reaction (ADE) equation, which can be written as

$$\frac{\partial C}{\partial t} + \vec{U} \cdot \vec{\nabla} C = D_m \triangle C + \frac{1}{\tau} f(C), \tag{1}$$

where the specific kinetics of the iodate arsenious acid (IAA) reaction is third order [20]: $f(C) = C^2(1 - C)$. C is the concentration of the autocatalytic reactant (iodide), normalized by the initial concentration of iodate ($C = [\mathrm{I}^-]/[\mathrm{IO_3}^-]_0$), τ is the reaction time, and D_m is the molecular diffusion. In the absence of flow, $\overline{U} = 0$, the balance between diffusion and reaction leads to a solitary wave of constant velocity V_χ and width l_χ [1,20,21], solutions of Eq. (1) given by

$$V_\chi = \sqrt{\frac{D_m}{2\tau}}, \qquad l_\chi = D_m / V_\chi. \tag{2}$$

Moreover, in the limit of small front thickness $l_\chi \ll 1$, Eq. (1) can be approximated by the eikonal equation

$$\vec{V_F} \cdot \vec{n} = \vec{U} \cdot \vec{n} + V_\chi + D_m \kappa, \tag{3}$$

where $\vec{n}$ is the normal component of the interface oriented toward the unburned regions, and κ is the curvature.

Here, we consider an autocatalytic reaction front propagation in the presence of an adverse flow in a heterogeneous porous medium. As a consequence of the flow opposing the front, static fronts have been found depending on the intensity of the the mean flow velocity $\overline{U}$ that is negative by convention. In previous studies [22–24] we have demonstrated that, depending on $\overline{U}$, the system display three propagating regimes. If the flow magnitude is high enough, the front recedes downstream. For an intermediate range of velocities, the front stops and adopts a stationary shape, hereby referred to as a "frozen state" (see also [25]). Finally, for a sufficiently low flow magnitude, the front manages to propagate upstream. In a previous work [24], we have demonstrated that the transition "frozen"-"upstream" can be understood to be a dynamical critical transition of a front interface in a quenched disorder (the back flow) subject to a forcing term (the chemical velocity). More particularly, we shed light on the fact that in the eikonal limit, the front line displays a spatial and temporal roughness belonging to the quenched-Kardar-Parisi-Zhang (qKPZ) [26–30] universality class.

Interface motion in quenched disorder has been a subject of immense importance in nonequilibrium statistical physics for decades. As controlled by a driving force, an interface shuffles between moving and pinned or static regimes. Close to a pinning-depinning transition point, the interface follows a burstlike motion referred to as an avalanche [31]. The spatiotemporal dynamics of avalanches exhibits scaling properties in the vicinity of a critical point, and it is a widely studied nonequilibrium phenomenon. Avalanches are observed in various systems, e.g., sand-pile [32,33], Barkhausen noise in ferromagnets [34], population dynamics, earthquakes [35], motion of vortices in superconductors, fracture propagation [36], fluid imbibition in porous media [37–39], or intermittent flow in amorphous materials [40–44]. Near the transition

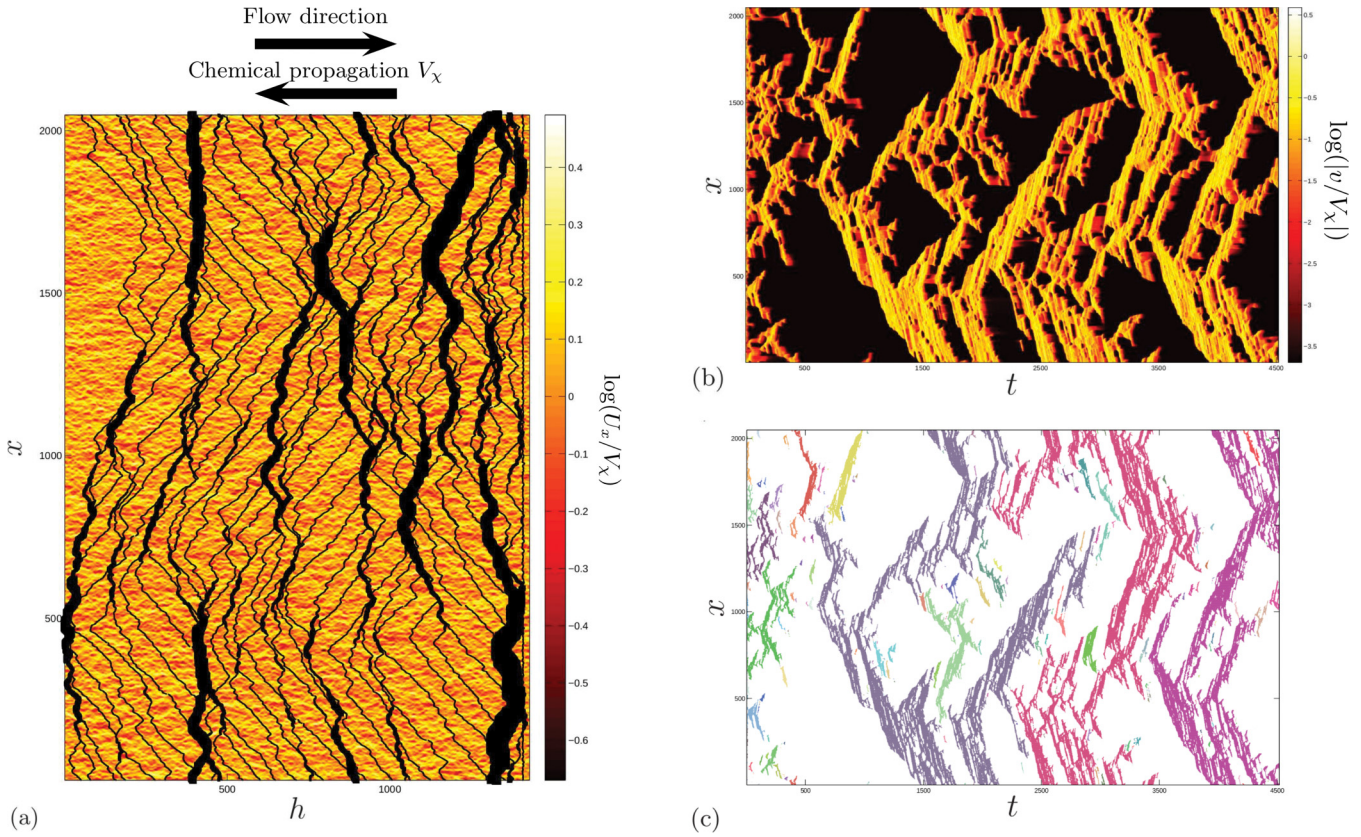

FIG. 1. (a) Front dynamic for $\epsilon = -1.13$. In black: front positions at different constant interval of time ($\delta t = 100\lambda/V_\chi$). In gray scale: logarithm of the normalized velocity field, $\log_{10}(U_x/V_\chi)$. The mean flow is oriented from left to right, and the chemical reaction propagates from right to left. The initial front location is flat and located at the rightmost end of the domain. (b) Spatiotemporal map of the logarithm of the normalized front velocity, $\log[|v(x,t)/V_\chi|]$. The mean front velocity is $V_f/V_\chi = 0.057$ (c) associated spatiotemporal identified clusters.

point, these systems show power-law distributed avalanches and universal behaviors. In this paper, we investigate the avalanche dynamics of an autocatalytic front in a heterogeneous medium at the transition from frozen states to upstream propagation.

II. NUMERICAL SIMULATION AND METHODS

We employ the same numerical procedure as in [23,24], which will be recalled briefly. We generate a permeability field according to a log-normal distribution [45,46], with correlation length λ and standard deviation $\sigma^2 = 0.5$. The velocity field is then determined by solving Darcy's equation with an imposed pressure gradient and using a two-relaxation-time lattice-Boltzmann scheme (TRT-LBM). In the last step, we solve the ADE equation (1) for the concentration with an initial flat front, using also a TRT-LBM scheme. All quantities are nondimensionalized using the correlation length λ, the chemical wave velocity V_χ, and the characteristic time λ/V_χ. We use $\epsilon = \overline{U}/V_\chi$ as the flow intensity control parameter. We define the front by extracting the isoconcentration $c = 0.5$. In this paper, the size of the system is 2048×2048 with a correlation length $\lambda = 5$. The critical velocity is found to be $\epsilon_c = \overline{U}/V_\chi = -1.17$.

Avalanche events are determined by evaluating the instant and local front velocity, $v(x,t) = \partial h/\partial t(x,t)$. From the spatiotemporal front velocity map represented in Fig. 1, we defined a velocity threshold $V_{\min}$ as the median of the nonzero velocities. From the spatiotemporal maps of front velocities, we obtain the associated cluster maps by applying this velocity threshold $V_{\min}$: a cluster defines a region where the front moves faster than $V_{\min}$. We reconstruct the associated spatial maps and spatial cluster maps. We then investigate the statistical properties of these clusters both in spatial and spatiotemporal spaces.

III. RESULTS

For each cluster, the following characteristics have been extracted: from the spatial maps, the size S, and from the smallest rectangle containing it, their length L and width W. From the spatiotemporal maps, we deduce the associated cluster duration T.

A. Distributions

We plot the probability distributions of these quantities in Fig. 2 for different distances to the critical ϵ_c (we have excluded clusters touching the inlet and the outlet). For statistical reasons, it was performed with different porous realizations. It can be seen that length, size, and duration distributions [$p(L)$, $p(S)$, and $p(T)$] follow reasonably a power-law decay

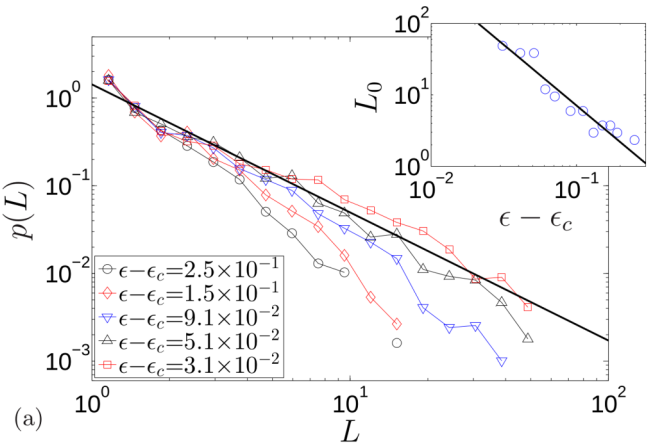

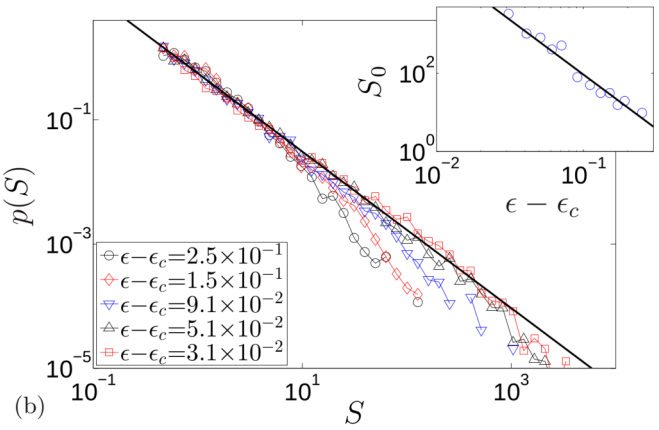

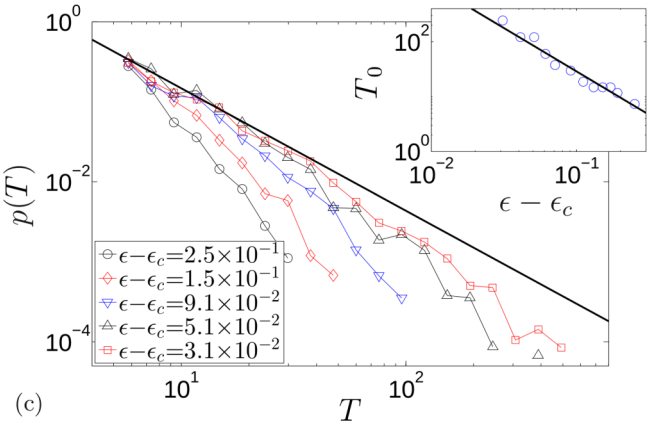

FIG. 2. Distribution of avalanche lengths (a), sizes (b), and durations (c) for different distances to the critical point $\epsilon_c = -1.17$. Insets: evolution of the corresponding cutoff as a function of the distance to the critical point $\epsilon - \epsilon_c$.

(with exponent $\tau_L = 1.46 \pm 0.10$, $\tau_S = 1.26 \pm 0.05$, and $\tau_T = 1.53 \pm 0.10$), with a cutoff at large sizes. Moreover, for each ϵ, the distributions can be well fitted by

$$p(L) \propto L^{-\tau_L} \exp(-L/L_0), \tag{4}$$

$$p(S) \propto S^{-\tau_S} \exp(-S/S_0), \tag{5}$$

$$p(T) \propto T^{-\tau_T} \exp(-T/T_0). \tag{6}$$

TABLE I. Exponents from simulations at the percolation transition and qKPZ theory.

Scaling law	Exponent	Simulation	qKPZ
$L_0 \propto (\epsilon - \epsilon_c)^{-\nu_L}$	$\nu_L = \nu$	1.70 ± 0.15	1.73
$W \propto L^{\zeta}$	ζ	0.74 ± 0.05	0.63
$L \propto T^{1/z}$	$1/z$	1.09 ± 0.1	1.00
$S \propto T^{\gamma}$	γ	1.79 ± 0.15	1.63
$S_0 \propto (\epsilon - \epsilon_c)^{-\nu_S}$	ν_S	2.80 ± 0.15	2.83
$T_0 \propto (\epsilon - \epsilon_c)^{-\nu_T}$	ν_T	1.64 ± 0.15	1.73
$p(L) \propto L^{-\tau_L}$	τ_L	1.46 ± 0.10	1.42
$p(S) \propto S^{-\tau_S}$	τ_S	1.26 ± 0.05	1.26
$p(T) \propto T^{-\tau_T}$	τ_T	1.53 ± 0.10	1.42

The cutoff sizes are defined as the intersection between the numerical distribution and the corresponding power law shifted below by a factor of 2. We found that this procedure is more robust than others, such as the maximum cluster size or the exponential fit. The insets of Fig. 2 provide the dependence of this cutoff size with $\epsilon - \epsilon_c$. The three cutoffs follow a power-law decay with $\epsilon - \epsilon_c$:

$$L_0 \propto (\epsilon - \epsilon_c)^{-\nu_L}, \tag{7}$$

$$S_0 \propto (\epsilon - \epsilon_c)^{-\nu_S}, \tag{8}$$

$$T_0 \propto (\epsilon - \epsilon_c)^{-\nu_T}. \tag{9}$$

All coefficients are displayed in Table I.

To validate our procedure, in Fig. 3 we show a remarkable data collapse using the exponents reported in Table I and a scaling ansatz of Eqs. (4)–(9). We note that other statistical properties of the clusters exhibit similar behaviors, such as W: $p(W) \propto W^{-\tau_W} \exp(-W/W_0)$ with $W_0 \propto (\epsilon - \epsilon_c)^{-\nu_W}$, which have not been plotted for the sake of conciseness.

B. Exponent relations

The dynamics involves many exponents. However, many of them are not independent and are related by some exponent relations that we will describe in this section.

Close to the critical point, the interface has a self-affine behavior in both space and time: the statistical properties of $h(ax,bt)$ are identical to $a^{\zeta} h(x,bt)$ and $b^{\zeta/z} h(ax,t)$, where ζ is the roughness exponent and z is the dynamical exponent. This property implies several relations, such as

$$W \propto L^{\zeta}, \tag{10}$$

$$S \propto L^{d+\zeta}, \tag{11}$$

$$T \propto L^{z}. \tag{12}$$

These scaling relations are tested in Fig. 4, where we compute $\langle W \rangle_L$ and $\langle S \rangle_T$. We can see that both quantities display a power-law growth at large L and T, respectively. In particular, from the self-affinity, we deduce $\langle S \rangle_T \propto T^{\gamma}$ with $\gamma = \frac{d+\zeta}{z}$. Following this argument, one can also relate the

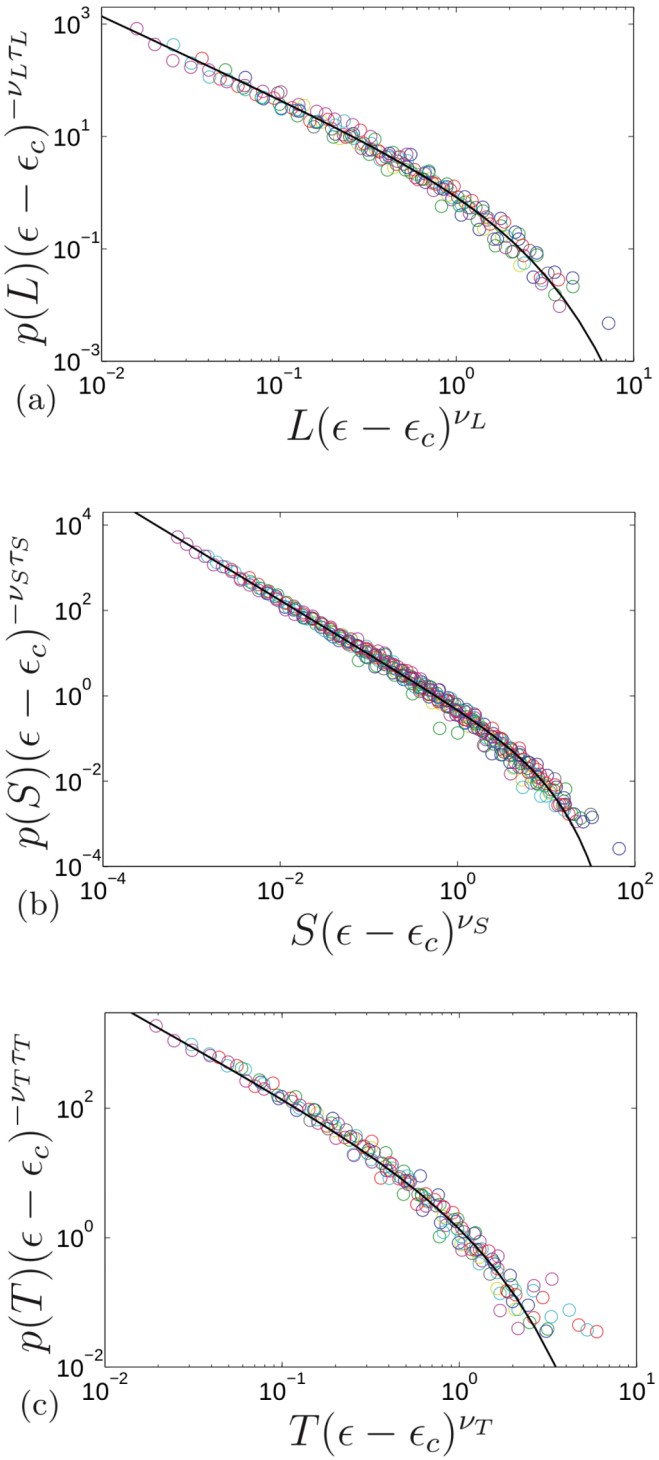

FIG. 3. Data collapse for lengths, sizes, and durations using the exponents of Table I and the scaling ansatz.

different cutoff exponents ν:

$$\nu_W = \nu_L\zeta,$$
$$\nu_S = \nu_L(d+\zeta),$$
$$\nu_T = \nu_L z.$$

Moreover, similar relations can be obtained for exponents τ by observing that given two quantities A and B related by $A \sim B^{\phi}$

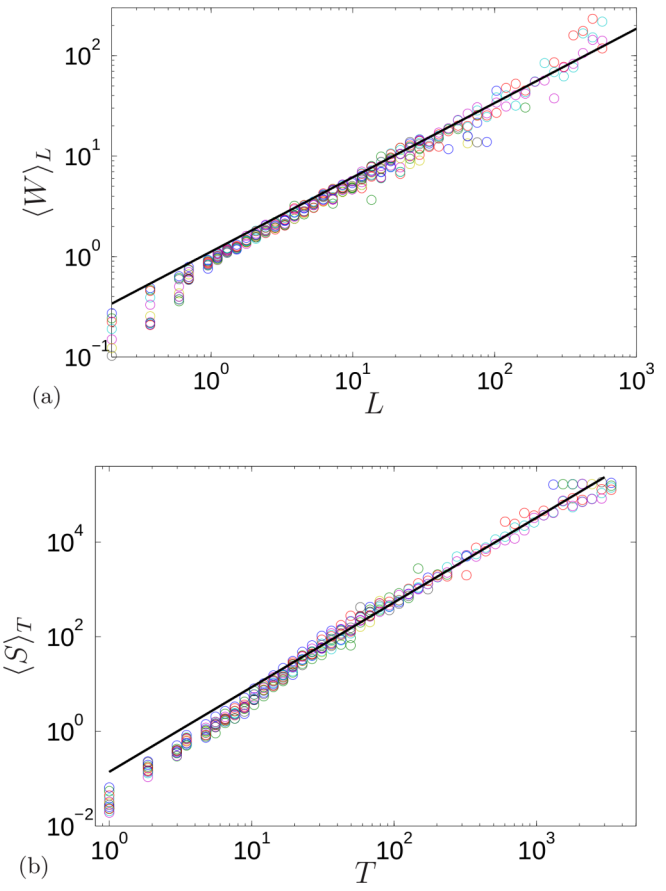

FIG. 4. Plots for (a) roughness and (b) area vs durations. Lines scale as (a) $\langle W\rangle_L \propto L^{\zeta}$ with $\zeta \approx 0.74$ and (b) $\langle S\rangle_T \propto T^{\gamma}$ with $\gamma \approx 1.79$.

and power-law distributed [$P(A) \propto A^{-\tau_A}$ and $P(B) \propto B^{-\tau_B}$], from $P(A)dA = P(B)dB$ follows $\tau_A \propto \phi\tau_B - (\phi - 1)$.

Finally, a relation for the exponent τ_S has been proposed in several studies [34,47–49]:

$$\tau_S = 2 - \frac{\zeta + 1/\nu_L}{d+\zeta}.$$

We conclude that if this last relation holds in our case, only three independent "universal" exponents remain: ν_L, ζ, and z. Table I summarizes the value of the exponents obtained by our fitting method. All the exponent relations are tested in Table II using the measured values of ν_L, ζ, and z. We observe

TABLE II. Exponents from simulations that can be validated by an exponent relation.

Exponent	Simulation	Scaling relation	Validation
γ	1.79 ± 0.15	$\gamma = (d+\zeta)/z$	1.90
ν_S	2.80 ± 0.15	$\nu_S = \nu(d+\zeta)$	2.96
ν_T	1.64 ± 0.15	$\nu_T = \nu z$	1.56
τ_L	1.46 ± 0.10	$\tau_L = d + 1 - 1/\nu$	1.41
τ_S	1.26 ± 0.05	$\tau_S = 2 - \frac{\zeta + 1/\nu}{d+\zeta}$	1.24
τ_T	1.53 ± 0.10	$\tau_T = \frac{(d-1/\nu)}{z} + 1$	1.45

a relatively good agreement for most of the exponents. In the next section, we discuss the origin of the small discrepancies.

IV. DISCUSSION AND CONCLUSION

In previous work, it has been shown that eikonal dynamics in the presence of disorder can be approximated by the qKPZ equation. Namely, the front interface follows

$$\frac{\partial h(x,t)}{\partial t} = l_\chi \nabla^2 h(x,t) + \frac{1}{2}[\nabla h(x,t)]^2 + \eta(x,h(x,t)) + f, \tag{13}$$

where $h(x,t)$ is the front location, and the quenched disorder can be related to the velocity field: $\eta(x,y) = -U_x(-x,y)/V_\chi + 1$. In one dimension, the critical exponents of the dynamics close to the depinning transition, $f \approx f_c$, are known with high precision thanks to a mapping with the directed percolation (DP) [26,50]. In particular, the DP exponents $\nu_\parallel = 1.733$ and $\nu_\perp = 1.097$ are related to the qKPZ exponents via $\zeta = \nu_\perp/\nu_\parallel$ and $\nu = \nu_\parallel$. Moreover, the spreading of a perturbation in an avalanche is ballistic, leading to $z = 1$. Using the scaling relations derived in the previous section, we can compute all the avalanche exponents as summarized in Table I. The agreement between the theoretical predictions and the measured results is good for both ν_L and z, while a significant discrepancy is observed for the roughness exponent. We note that this discrepancy may propagate onto the other exponents by means of some exponent relations. Some indications seem to suggest that the roughness exponent is not correctly evaluated. For instance, the roughness could be alternatively deduced by the ratio $\zeta = \nu_S/\nu - 1 \simeq 0.65$, which is closer to the expected 0.63 than the direct measure 0.74. This anomaly can have two origins: (i) the present disorder field differs from the usual one as it is not short-ranged and isotropic, and (ii) the geometry of the interface is measured in the moving phase while the DP mapping works in the quasistatic limit, as in Atis *et al.* [24]. To assess the first hypothesis, we study in the Appendix the DP mapping using our velocity field as the quenched disorder. Using this method, one can extract the correct average exponent ∼0.633, however we note that strong statistical fluctuations are still present at large sizes (with a statistical error of 10% for sizes up to 8096×8096, while the dynamical simulations are only 2048×2048). On the other hand, we recall that in Atis *et al.* [24], the roughness exponent of the moving front was significantly larger (∼0.8) with respect to the quasistatic one (see also [26]). We believe that both effects contribute to overestimate the roughness of the front. We may thus conclude that the behavior of the quenched eikonal equation is consistent with the quenched KPZ universality class. In analyzing the data of such models, particular care should be taken for an estimation of the roughness exponent, which is particularly sensitive to finite-size effects, especially in the moving phase. Finally, we should mention that we have tried to characterize the avalanche dynamic experimentally with the setup described in Atis *et al.* [24]. As preliminary results, we have indeed observed a power-law distribution for burst size and duration, which would support the contention of an avalanche dynamic. However, the lack of good statistics (system size and a large amount of realizations) did not allow for a precise determination of the exponents.

ACKNOWLEDGMENTS

The authors would like to thank Mikko Alava, Alex Hansen, Pierre Le Doussal, and Kay Wiese for useful discussions, and the Agence Nationale de la Recherche for financial support of the project LaboCothep ANR-12-MONU-0011.

APPENDIX: DIRECTED PERCOLATION

Other than the roughness exponent ζ, which is higher, the results show that all the exponents are close to the qKPZ ones. A possible explanation for this discrepancy could arise from our particular disorder field, which is correlated and anisotropic. To assess this possibility, we revisit the directed percolation depinning (DPD) model in our case.

We first recall briefly the origin of the directed percolation mapping. As discussed in previous work [23], the interface is able to propagate wherever the local flow velocity is lower than the chemical velocity (i.e., $|U| < V_\chi$), but it can be blocked if the velocity is higher. A necessary condition to be pinned is the existence of a blocking ($|U| > V_\chi$) path transverse to the flow direction, which defines a percolation criterion. We note that one can understand qualitatively the avalanche characteristics from the DPD model. Close to the critical point, there are many paths that are almost blocking (percolating). The front will then stop for some time along these paths. An avalanche event is then characterized by two successive blocking paths. We thus expect that the roughness as well as the size distributions of the avalanches are described by the directed percolation model.

First, we remark that the argument used here is the dual version of the one we employed earlier in [23], where we were looking for nonblocking areas percolating perpendicular to the front. Another important remark is that the percolation is directed because the height is assumed to be a function of the transverse coordinate [$h(x,t)$], but also because the local slopes are imposed by the eikonal equation. Indeed, in the high-speed regions, the eikonal equation imposes only two admissible slopes of a static front:

$$\vec{0} = \vec{U}(x,h) \cdot \vec{n} + V_\chi, \tag{A1}$$

which implies

$$\frac{\partial h}{\partial x} = \pm\sqrt{\left(\frac{\bar{U} + \delta U_y(x,h)}{V_\chi}\right)^2 - 1}, \tag{A2}$$

where we have neglected the transverse component of the flow velocity.

The directed percolation criterion is met once there is a transverse path along which the velocity is always higher than V_χ. In other words, the criterion implies the existence of a path $\mathcal{C} \in \Omega$ such that

$$\min_{\mathcal{C}} (U_y(h,x)) > V_\chi,$$

where Ω denotes the ensemble of paths connecting one side to the other, satisfying Eq. (A2). This condition depends on both the mean velocity and the chemical velocity. It is convenient,

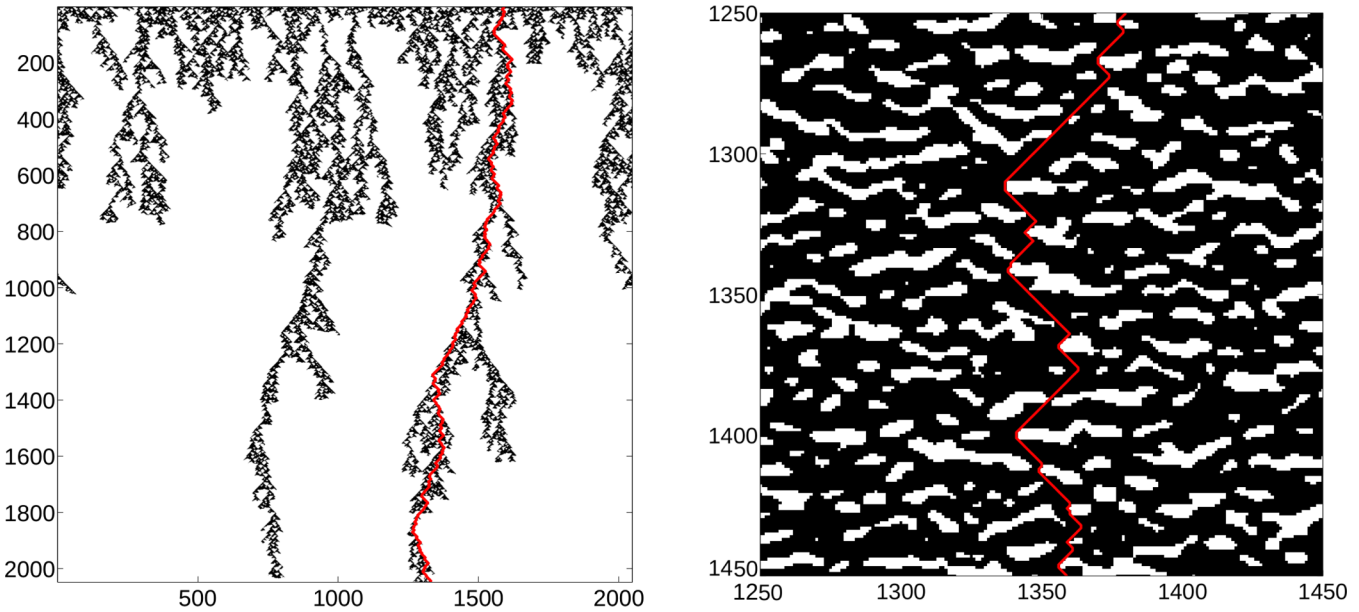

FIG. 5. Example of the transfer-matrix algorithm applied to the velocity field at the percolation threshold. Left: in black are the points connected to the top border by a percolating path. Right: binarized velocity field (black, $|U| > V_\chi$; white, $|U| < V_\chi$). In both figures, the red path corresponds to the first barrier from left to right.

however, as in the directed percolation algorithm, to simplify this condition by assuming $\frac{\partial h}{\partial x} = \pm 1$.[1] We also remark that this procedure can also be viewed as a simplified barrier invariant manifold (BIM) introduced by several authors [51,52].

One convenient method to determine the directed percolation threshold consists in evaluating the maximum over all the minimum velocity along each path. That can be obtained from a standard "min-max" transfer matrix algorithm (see [23,53]): Defining the matrix $C_{i,j}$ as being the maximum of the minimum velocity among the entire directed path connecting the first line to the point (i,j), this matrix is determined recursively line by line:

$$C_{i+1,j} = \min\{\max[C_{i,j-1}, C_{i,j}, C_{i,j+1}], U_{i+1,j}\}.$$

The percolation threshold is then given for the chemical velocity equal to the maximum of C along the last line (nI):

$$V_\chi{}^c = \max_j C(nI, j).$$

Once the end point of the barrier has been identified, we reconstruct the path $J(i)$ iteratively from the last line nI to the first one by choosing the following:

$$J(i-1) \in \{J(i)-1; J(i); J(i)+1\} \text{ with } C_{i-1,J(i-1)} > V_\chi{}^c.$$

Of course, in principle there could be many choices. However, since the chemical front is propagating leftward and since we want the first-met barrier, we pick always the most rightward point among the possibilities. In other words, we choose in priority order $J(i)+1$, $J(i)$, and $J(i)-1$.

We can then use the algorithm to estimate the frozen front for an arbitrary velocity field. By applying this algorithm on the velocity field obtained from the simulation, we obtained a roughness ranging between 0.6 and 0.7. Unfortunately, in order to be more precise, a better statistics is required (a greater number of realizations and with a larger domain size, etc.). Solving Darcy flow for each system would require a large amount of CPU time. To overcome this problem, we generate the velocity field stochastically using its Fourier transform obtained from the linear expansion of the equations [45,46]

$$\hat{u}_x(k_x,k_y) = \hat{f}\frac{k_y^2}{k_x^2+k_y^2} = f_0\hat{W}\frac{k_y^2}{k_x^2+k_y^2}e^{-\frac{k_x^2+k_y^2}{k_0^2}}, \qquad \text{(A3)}$$

where a caret denotes the Fourier transform, and W denotes an uncorrelated white noise distribution.

Figure 5 displays an example of path determination that has a roughness of 0.67. By these means, we have been able to compute the barrier front for around 1000 velocity fields of domain sizes 8096. We have plotted in Fig. 6 the average two-point correlation function $W(l) = \sqrt{\langle [h(y) - h(y+l)]^2 \rangle}$ for a velocity distributed according to Eq. (A3) (red) and a white noise (blue). The comparison is instructive as it shows that the roughness exponent is compatible with the DPD universality class. However, it shows that the scaling law is valid over a rather short window size, $l \in [5\lambda, 50\lambda]$. Moreover, considering the roughness distribution of each realization, we observe that even though the average is rather good, $\langle H \rangle = 0.63$, the standard deviation is significant, $\sigma(H) = 0.04$.

We conclude that with this particular velocity field correlation, the roughness exponent of the DPD universality class should be recovered. However, we note that the presence of correlations reduces significantly the windows of scales over which the scaling law is valid and thus the dispersion of the results despite the large domain sizes and the number of realizations.

[1]The model then consists in assuming the velocity is equal to $\sqrt{2}V_\chi$ in the high-velocity zones.

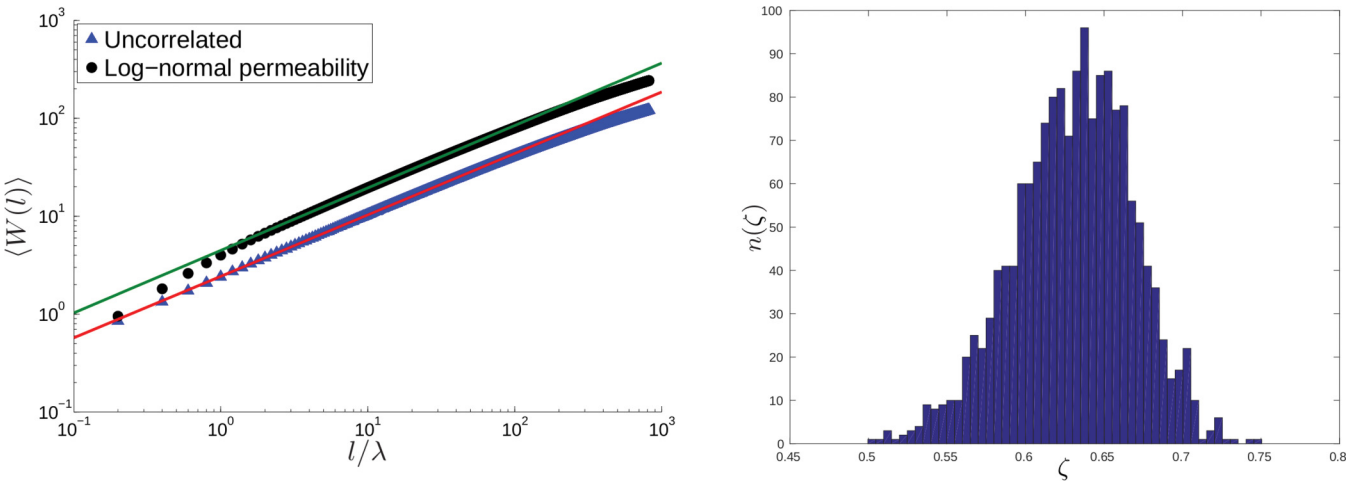

FIG. 6. Left: two-point correlation function $W(l) = \sqrt{\langle [h(y) - h(y+l)]^2 \rangle}$ of the directed percolation path for two types of disorder. Blue triangles: uncorrelated white noise. Green circles: velocity field from the log-normal permeability distribution. The two lines correspond to the fitted scaling $W(l) \propto l^{\zeta}$. Right: distribution roughness exponent measured for the log-normal permeability. The mean of the distribution is $\langle \zeta \rangle = 0.63$ and the standard deviation is $\mathrm{std}(\zeta) = 0.04$.

[1] S. K. Scott, in *Oscillations, Waves, and Chaos in Chemical Kinetics*, edited by O. C. Primers (Oxford University Press, Oxford, 1994).
[2] R. A. Fisher, Ann. Eugenics **7**, 355 (1937).
[3] A. N. Kolmogorov, I. G. Petrovskii, and N. S. Piskunov, Bjul. Moskovskogo Gos. Univ. **1**, 1 (1937).
[4] Y. Zeldovich and D. Frank-Kamenetskii, Zh. Fiz. Khim. **12**, 100 (1938).
[5] B. Audoly, H. Berestycki, and Y. Pomeau, C. R. Acad. Sci. Paris, Ser. II B **328**, 255 (2000).
[6] M. Abel, A. Celani, D. Vergni, and A. Vulpiani, Phys. Rev. E **64**, 046307 (2001).
[7] B. F. Edwards, Phys. Rev. Lett. **89**, 104501 (2002).
[8] M. Leconte, J. Martin, N. Rakotomalala, and D. Salin, Phys. Rev. Lett. **90**, 128302 (2003).
[9] M. Leconte, J. Martin, N. Rakotomalala, and D. Salin, J. Chem. Phys. **120**, 7314 (2004).
[10] M. S. Paoletti and T. H. Solomon, Phys. Rev. E **72**, 046204 (2005).
[11] M. S. Paoletti and T. H. Solomon, Europhys. Lett. **69**, 819 (2005).
[12] B. F. Edwards, Chaos **16**, 043106 (2006).
[13] A. Pocheau and F. Harambat, Phys. Rev. E **73**, 065304 (2006).
[14] D. A. Vasquez, Phys. Rev. E **76**, 056308 (2007).
[15] M. Leconte, N. Jarrige, J. Martin, N. Rakotomalala, D. Salin, and L. Talon, Phys. Fluids **20**, 057102 (2008).
[16] M. Kaern and M. Menzinger, J. Phys. Chem. B **106**, 3751 (2002).
[17] I. V. Koptyug, V. V. Zhivonitko, and R. Z. Sagdeev, J. Phys. Chem. B **112**, 1170 (2008).
[18] M. E. Schwartz and T. H. Solomon, Phys. Rev. Lett. **100**, 028302 (2008).
[19] J. Martin, N. Rakotomalala, L. Talon, and D. Salin, Phys. Rev. E **80**, 055101 (2009).
[20] A. Hanna, A. Saul, and K. Showalter, J. Am. Chem. Soc. **104**, 3838 (1982).
[21] M. Böckmann and S. C. Müller, Phys. Rev. Lett. **85**, 2506 (2000).
[22] S. Atis, S. Saha, H. Auradou, D. Salin, and L. Talon, Phys. Rev. Lett. **110**, 148301 (2013).
[23] S. Saha, S. Atis, D. Salin, and L. Talon, Europhys. Lett. **101**, 38003 (2013).
[24] S. Atis, A. K. Dubey, D. Salin, L. Talon, P. Le Doussal, and K. J. Wiese, Phys. Rev. Lett. **114**, 234502 (2015).
[25] T. Gueudré, A. K. Dubey, L. Talon, and A. Rosso, Phys. Rev. E **89**, 041004 (2014).
[26] L. H. Tang and H. Leschhorn, Phys. Rev. A **45**, R8309(R) (1992).
[27] A.-L. Barabasi and H. E. Stanley, *Fractal Concepts in Surface Growth* (Cambridge University Press, Cambridge, 1995).
[28] L.-H. Tang, M. Kardar, and D. Dhar, Phys. Rev. Lett. **74**, 920 (1995).
[29] H. Leschhorn, T. Nattermann, S. Stepanow, and L.-H. Tang, Ann. Phys. **509**, 1 (1997).
[30] A. Rosso and W. Krauth, Phys. Rev. Lett. **87**, 187002 (2001).
[31] A. Rosso, P. Le Doussal, and K. J. Wiese, Phys. Rev. B **80**, 144204 (2009).
[32] P. Bak, C. Tang, and K. Wiesenfeld, Phys. Rev. A **38**, 364 (1988).
[33] M. Paczuski, S. Maslov, and P. Bak, Phys. Rev. E **53**, 414 (1996).
[34] S. Zapperi, P. Cizeau, G. Durin, and H. E. Stanley, Phys. Rev. B **58**, 6353 (1998).
[35] E. A. Jagla, F. P. Landes, and A. Rosso, Phys. Rev. Lett. **112**, 174301 (2014).
[36] D. Bonamy, S. Santucci, and L. Ponson, Phys. Rev. Lett. **101**, 045501 (2008).
[37] M. Alava, M. Dubé, and M. Rost, Adv. Phys. **53**, 83 (2004).
[38] K. J. Måløy, S. Santucci, J. Schmittbuhl, and R. Toussaint, Phys. Rev. Lett. **96**, 045501 (2006).
[39] S. Santucci, R. Planet, K. J. Maloyy, and J. Ortin, Europhys. Lett. **94**, 46005 (2011).
[40] J.-C. Baret, D. Vandembroucq, and S. Roux, Phys. Rev. Lett. **89**, 195506 (2002).

[41] J. Lin, T. Gueudré, A. Rosso, and M. Wyart, Phys. Rev. Lett. **115**, 168001 (2015).
[42] T. Chevalier and L. Talon, Phys. Rev. E **91**, 023011 (2015).
[43] T. Chevalier and L. Talon, Eur. Phys. J. E **38**, 76 (2015).
[44] C. Liu, E. E. Ferrero, F. Puosi, J.-L. Barrat, and K. Martens, Phys. Rev. Lett. **116**, 065501 (2016).
[45] L. Gelhar and C. Axness, Water Resour. Res. **19**, 161 (1983).
[46] L. Talon, J. Martin, N. Rakotomalala, D. Salin, and Y. Yortsos, Water Resour. Res. **39**, 1135 (2003).
[47] O. Narayan and D. S. Fisher, Phys. Rev. B **48**, 7030 (1993).
[48] P. Le Doussal and K. J. Wiese, Phys. Rev. E **79**, 051106 (2009).
[49] L. E. Aragón, E. A. Jagla, and A. Rosso, Phys. Rev. E **85**, 046112 (2012).
[50] L. A. N. Amaral, A.-L. Barabási, S. V. Buldyrev, S. T. Harrington, S. Havlin, R. Sadr-Lahijany, and H. E. Stanley, Phys. Rev. E **51**, 4655 (1995).
[51] D. Bargteil and T. Solomon, Chaos **22**, 037103 (2012).
[52] K. A. Mitchell and J. R. Mahoney, Chaos **22**, 037104 (2012).
[53] A. Hansen and S. Roux, J. Phys. A **20**, L873 (1987).